Magnetic properties and domain structure of ultrathin yttrium iron garnet/Pt bilayers

J. Mendil,[1] M. Trassin,[1] Q. Bu,[1] J. Schaab,[1] M. Baumgartner,[1] C. Murer,[1] P. T. Dao,[1] J. Vijayakumar,[2] D. Bracher,[2]
C. Bouillet,[3] C. A. F. Vaz,[2] M. Fiebig,[1] and P. Gambardella[1]

[1]*Department of Materials, ETH Zurich, CH-8093 Zurich, Switzerland*

[2]*Swiss Light Source, Paul Scherrer Institut, CH-5232 Villigen PSI, Switzerland*

[3]*Institut de Physique et Chimie des Matériaux de Strasbourg (IPCMS), UMR 7504 CNRS, Université de Strasbourg, 67034 Strasbourg, France*

We report on the structure, magnetization, magnetic anisotropy, and domain morphology of ultrathin yttrium iron garnet (YIG)/Pt films with thickness ranging from 3 to 90 nm. We find that the saturation magnetization is close to the bulk value in the thickest films and decreases at low thickness with a strong reduction below 10 nm. We characterize the magnetic anisotropy by measuring the transverse spin Hall magnetoresistance as a function of applied field. Our results reveal strong easy-plane anisotropy fields of the order of 50–100 mT, which add to the demagnetizing field, as well as weaker in-plane uniaxial anisotropy ranging from 10 to 100 μT. The in-plane easy-axis direction changes with thickness but presents also significant fluctuations among samples with the same thickness grown on the same substrate. X-ray photoelectron emission microscopy reveals the formation of zigzag magnetic domains in YIG films thicker than 10 nm, which have dimensions larger than several 100 μm and are separated by achiral Néel-type domain walls. Smaller domains characterized by interspersed elongated features are found in YIG films thinner than 10 nm.

I. INTRODUCTION

Yttrium iron garnet (YIG) thin films have attracted considerable interest in the field of spintronics due to the possibility of converting magnon excitations into spin and charge currents flowing in an adjacent nonmagnetic metal (NM) layer. Spin currents in YIG/NM bilayers have been excited thermally (spin Seebeck effect) [1–4], dynamically (spin pumping) [5–8], or by means of the spin Hall effect [9–13]. In the last case, a charge current in the NM generates a transverse spin current that is either absorbed or reflected at the interface with YIG. This leads to a variety of interesting effects such as the spin Hall magnetoresistance (SMR) [14–17] and current-induced spin-orbit torques [18–20], which can be used to sense and manipulate the magnetization. For the latter purpose, it is desirable to work with thin magnetic films in order to achieve the largest effect from the interfacial torques.

For a long time, the growth of YIG has been accomplished by liquid phase epitaxy, which offers excellent epitaxial quality and dynamic properties such as low damping and a rich spin-wave spectrum. The magnetic properties of these bulklike samples, including the magnetocrystalline anisotropy [21,22] and magnetic domain structure [23–25], have been extensively characterized in the past. However, with rare exceptions [26], samples grown by liquid phase epitaxy usually have thicknesses in the micrometer to millimeter range. Recent developments in oxide thin-film growth give access to the submicrometer range by employing techniques such as laser molecular beam epitaxy [27], sputtering [28,29], and pulsed laser deposition (PLD) [30–37], which allow for growing good quality films with thickness down to the sub-100-nm range [28,29,35–37] and even below 10 nm [27,33,34].

Since the thickness as well as structural and compositional effects have a large influence on the magnetic behavior, these developments call for a detailed characterization of the magnetic properties of ultrathin YIG films. Several characteristic quantities, which are of high relevance for YIG-based spintronics, have been found to vary in films thinner than 100 nm. For instance, a reduction of the saturation magnetization [29,35–40] is typically observed in YIG films with thickness down to 10 nm, which has been ascribed to either thermally induced stress [38], lack of exchange interaction partners at the interface [36], or stoichiometric variations [29,37,39,40]. Furthermore, an increase of the damping [33–35,41] as well as a decreased spin-mixing conductance [42,43] have been found in ultrathin YIG. Finally, the emergence of unexpected magnetocrystalline anisotropy was reported for films of different orientations grown on gadolinium gallium garnet (GGG) and yttrium aluminum garnet (YAG). The magnetic anisotropy was investigated by the magneto-optical Kerr effect in GGG/YIG(111) [27,36] and by ferromagnetic resonance in GGG/YIG(111) [31], GGG/YIG(001) [32], and YAG/YIG(001) [28]. Whereas all these studies address important magnetic characteristics in the sub-100-nm range, only a few studies [33,34] explore the ultrathin-film regime below 10 nm. This thickness range is highly relevant for efficient magnetization manipulation using current-induced interfacial effects as well as for strain engineering, since strain and its gradients relax after 10–20 nm. Finally, a comprehensive knowledge of the domain and domain-wall structure in the thin-film regime is lacking. Recent studies on magnetic domains address only bulk [25], several-micrometer-thick [44] or hundreds-of-nanometers-thick [45] YIG films.

In this work, we present a systematic investigation of the structure, saturation magnetization, magnetic anisotropy, and

TABLE I. Overview of the three sample series used for anisotropy characterization using SMR and domain structure using XPEEM where t_{Pt} and t_{YIG} refer to the Pt and YIG thickness, respectively. The numbers in parentheses refer to the thickness in unit cells of YIG (1 unit cell = 1.238 nm [46]).

	t_{Pt} (nm)	t_{YIG} (nm, unit cells)						
SMR 1	3	3.4	4.6	6.2	7.3	9	29	90
		(2.7)	(3.7)	(5.0)	(5.9)	(7.3)	(23.4)	(72.7)
SMR 2	3		3.7	5.6	6.2	6.8	7.4	12.4
			(3.0)	(4.5)	(5.0)	(5.5)	(6.0)	(10.0)
XPEEM	1.9			3.7	8.7	12.4	28.5	86.7
				(3.0)	(7.0)	(10.0)	(23.0)	(70.0)

magnetic domains of YIG/Pt films grown on GGG substrates by PLD as a function of YIG thickness from $t_{YIG} = 3.4$ to $t_{YIG} = 90$ nm. By combining x-ray diffraction (XRD), transmission electron microscopy (TEM), atomic force microscopy (AFM), and x-ray absorption spectroscopy, we show that our films possess high crystalline quality and smooth surfaces with no detectable interface mixing throughout the entire thickness range. The saturation magnetization, investigated using a superconducting quantum interference device (SQUID), shows values close to bulk for thick films and a gradual reduction at lower thicknesses. We probe the magnetic anisotropy electrically by means of SMR and find an easy-plane and uniaxial in-plane anisotropy with a nonmonotonic variation of the in-plane orientation of the easy axis and the magnitude of the effective anisotropy field. Finally, we investigate the domain structure using x-ray photoelectron emission microscopy (XPEEM), evidencing significant changes in the domain structure above and below $t_{YIG} = 10$ nm. Our results provide a basis for understanding the behavior of spintronic devices based on YIG/Pt with different YIG thickness.

II. GROWTH AND STRUCTURE

We prepared three sample series consisting of GGG/YIG(t_{YIG})/Pt bilayers with Pt thickness set to 3 nm in the first two series for optimal SMR measurements and 1.9 nm in the third series to allow for surface-sensitive XPEEM measurements while avoiding charging effects. The YIG thickness, t_{YIG}, varies from 3.4 to 90 nm. An overview of the samples and their thickness in nanometers and YIG unit cells can be found in Table I. The samples have been grown *in situ* on (111)-oriented GGG substrates using an ultrahigh-vacuum PLD system combined with dc magnetron sputtering (base pressure 10^{-8} mbar, 10^{-10} mbar, respectively). The YIG was grown by PLD at a growth pressure of 10^{-1} mbar and temperature of 720°C using an excimer KrF laser (wavelength 248 nm) at a repetition rate of 8 Hz and 1.45 J/cm^2 fluence. Reflection high-energy electron diffraction (RHEED) was used to monitor the growth rate *in situ*. After cooling down under a 200-mbar O_2 atmosphere, the GGG/YIG films were transferred to the sputtering chamber without breaking the ultrahigh vacuum, where Pt was deposited at room temperature under 10^{-2} mbar Ar pressure. Finally, for electrical transport measurements, the YIG(t_{YIG})/Pt(3) series were patterned into Hall bar structures using optical lithography followed by Ar-ion milling. The Hall bars are oriented parallel to the [1$\bar{1}$0] crystal direction

and are 50 μm wide, with a separation of the Hall arms of 500 μm.

The crystalline quality and epitaxial strain of the GGG/YIG(111) films were investigated using XRD to obtain θ-2θ diffraction scans and reciprocal space maps. The interface quality was probed using scanning TEM (STEM), energy dispersive x-ray spectroscopy (EDS), and electron-energy-loss spectroscopy (EELS) in order to resolve the elemental composition, whereas the thin-film topography was investigated using AFM in both contact and tapping mode.

The YIG films are single-phase epitaxial layers with (111) orientation, as indicated by the diffraction peaks corresponding to the (111) planes in the diffraction pattern. The x-ray diffractograms for three selected YIG thicknesses are shown in Figs. 1(a)–1(c). Kiessig thickness fringes indicate the homogeneous growth and high interface quality. The observed periodicity matches the thicknesses determined by x-ray reflectivity. To further investigate the crystalline quality and the interfacial strain states of the YIG films, we recorded reciprocal space maps around the (664) and (486) diffractions for both YIG and the GGG substrate. These maps allow us to probe the strain state of the films along the two inequivalent [11$\bar{2}$] and [1$\bar{1}$0] in-plane directions. A coherent strain state of the films was evidenced for all thicknesses considered. The good lattice matching between YIG and GGG results in high-quality epitaxial growth and no detectable strain relaxation, as shown by the alignment of the diffraction points along both [11$\bar{2}$] and [1$\bar{1}$0] orientations. The reciprocal space maps measured on a 99-nm-thick YIG film are shown in Figs. 1(d) and 1(e).

Figures 1(f) and 1(g) show high-resolution STEM images of the two interfaces and a TEM image of the full stack in the inset. The corresponding chemical profiles across the interfaces probed by EDS are shown in Figs. 1(h) and 1(i). The EDS profiles indicate a moderate interdiffusion of Fe, Y, and Pt within a range of 2 nm at the YIG/Pt interface and of Gd and Ga into YIG within a range of about 4 nm at the GGG/YIG interface. Both values are in agreement with recent findings [39,47]. The smaller diffusion range at the YIG/Pt interface is consistent with the low power and lower deposition temperature (room temperature) of Pt compared to the deposition of YIG on GGG. The moderate diffusion of Ga and Gd into the YIG film is also in agreement with previous reports [29,39]. The EELS analysis, shown in Fig. 2, confirms the moderate diffusion of Fe in the Pt. In order to gain information on the evolution of the local Fe environment across the YIG/Pt interface, we calculated the intensity ratio
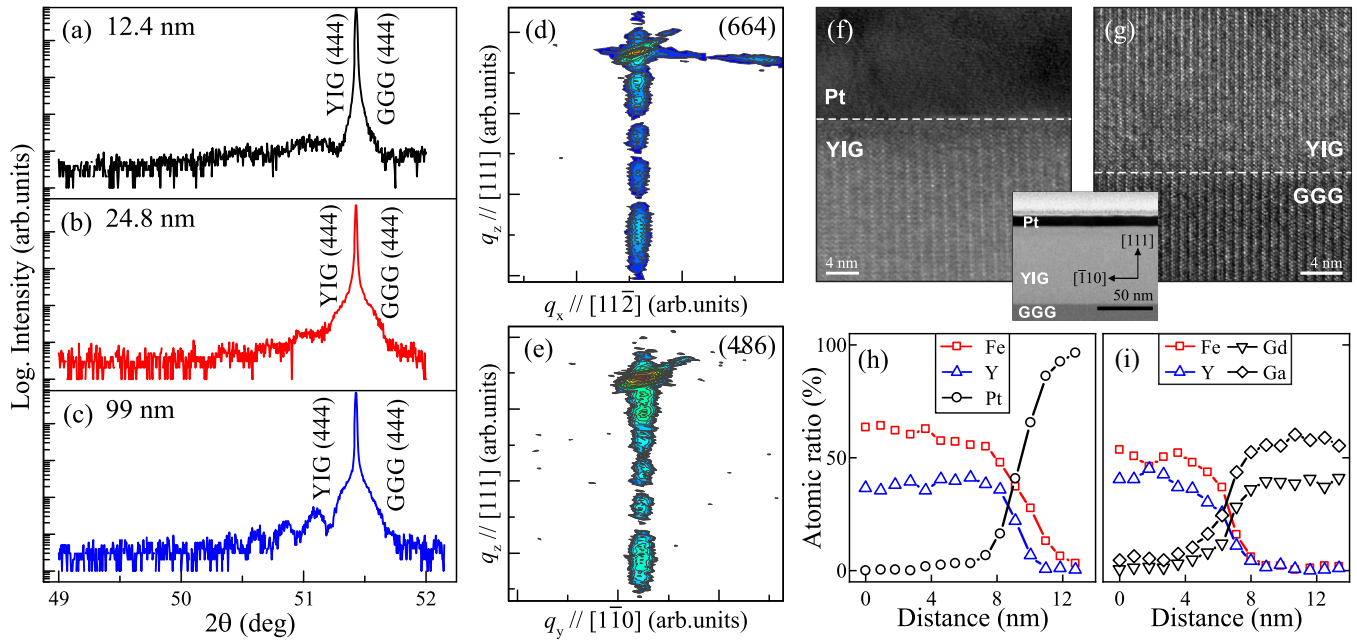
FIG. 1. (a–c) Structural characterization of GGG/YIG(111) films of different thickness by θ-2θ scans using XRD. (d, e) Reciprocal space maps around the (664) and (486) diffraction peaks. The oscillations in the θ-2θ and q_z scans are thickness oscillations. The thickness derived from these measurements agrees with that measured using x-ray reflectivity. (f, g) High-resolution STEM image of the two interfaces in the stack GGG/YIG(72)/Pt(9). The inset shows a cross section of the full stack. (h, i) Elemental profiles across the YIG/Pt and YIG/GGG interfaces measured by EDS.

of the Fe L_3 and L_2 white lines from the Fe EELS spectra measured within the YIG film (black dot in Fig. 2) and at two different positions near the YIG/Pt interface (red and blue dots). In YIG, the L_3/L_2 ratio is 5.64, which is consistent with an Fe^{3+} oxidation state, as found, e.g., in Fe_2O_3 [48]. On the Pt side of the YIG/Pt interface, the L_3/L_2 ratio decreases to 4.24, which is in between the values found for Fe and FeO. This change of electronic valence confirms the presence of Fe in the interfacial Pt layer. We note that the absence of Fe^{3+} in the Pt further excludes measurement artifacts due to sample preparation for TEM, such as Pt redeposition. The AFM

measurements substantiate the low roughness expected from the x-ray reflectivity and the observation of Kiessig fringes in the diffraction spectra. Figure 3(a) shows an AFM image over an area of 3×3 μm^2 of a 28.5-nm-thick GGG/YIG film. The measured roughness is in the range of 1 Å and is independent of the YIG thickness, as shown in Fig. 3(b).

III. SATURATION MAGNETIZATION

Figure 4(a) shows the saturation magnetization (M_s) of the unpatterned YIG(t_{YIG})/Pt(3) bilayers measured by SQUID (sample series SMR 1 and SMR 2 in red and grey, respectively). For each thickness, we observe a hysteretic in-plane magnetization with coercivity smaller than 0.5 mT, as illustrated for YIG(9)/Pt(3) in Fig. 4(b). The thickest sample, YIG(90)/Pt(3), has a saturation magnetization of $\mu_0 M_s =$ 153 mT, which is close to the bulk value of $\mu_0 M_{s,bulk} =$ 180 mT at room temperature [49]. The reduction of M_s compared to the bulk was also observed in other studies of
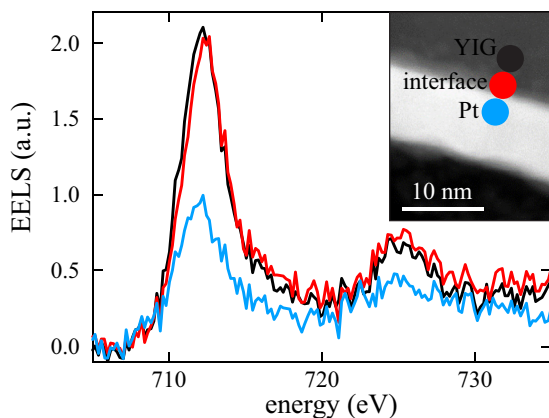

FIG. 2. Comparison of the Fe $L_{2,3}$ spectra measured by EELS across the YIG/Pt interface. The spectra, shown after background subtraction, have been averaged on 3-nm-long line scans for each region of interest, as labeled in the inset with colored dots. The probe beam diameter is 0.15 nm.
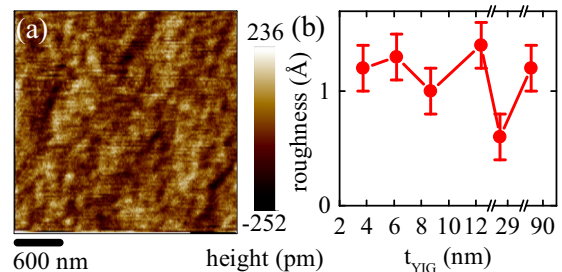

FIG. 3. (a) AFM image of YIG(28.5)/Pt(3). (b) Root-mean-square roughness as a function of YIG thickness measured by AFM.
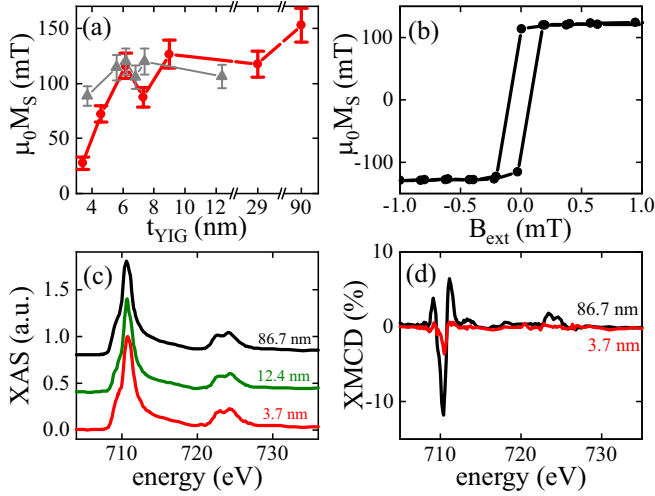
FIG. 4. (a) M_s as a function of YIG thickness measured by SQUID for sample series SMR 1 (red) and SMR 2 (grey). (b) Magnetic hysteresis of YIG(9)/Pt(3) as a function of in-plane magnetic field. (c) X-ray absorption spectra of YIG(3.7,12.4,86.7)/Pt(1.9). Each line represents the sum of two spectra acquired with positive and negative circular x-ray polarization. The spectra are shifted vertically by a constant offset for better visibility. (d) XMCD spectra for the thickest and thinnest samples obtained by taking the difference between two absorption spectra acquired with positive and negative circular x-ray polarization. The spectra were acquired on homogeneously magnetized domains using the XPEEM setup.

YIG films grown by PLD [31,36,50,51]. This reduction has been ascribed to the different percentage of Fe vacancies at the tetrahedral or octahedral sites [31], the lack of exchange interaction partners for atoms at the interface [36], strain relaxation due to a slight lattice mismatch of the substrate and YIG [50], as well as to the presence of Fe and O vacancies [51]. Furthermore, we observe a decreasing trend for M_s at lower YIG thicknesses, with a steeper reduction below 10 nm. Our thinnest sample ($t_{YIG} = 3.4$ nm) has $\mu_0 M_s = 27$ mT, which is only 15% of the bulk saturation magnetization. Previous studies reported a decreasing trend of M_s already for thicknesses larger than 10 nm [29,36,39,40,50].

The reduction of the YIG magnetization in thin films has been often modeled as a magnetically dead layer. For example, by extrapolating the areal magnetization as a function of thickness to the point where no surface magnetization would be present, Mitra *et al.* [39] inferred a 6-nm-thick dead layer for YIG films in the 10–50-nm thickness range. A similar extrapolation of our M_s data for samples with thickness of 9 nm and above would lead to a 4.3-nm-thick dead layer. However, our data evidence a finite magnetization below 4.3 nm, contradicting the assumption of an abrupt magnetically dead layer at the GGG/YIG interface. Instead, we conclude that a gradual reduction of M_s occurs at thicknesses below 10 nm, which may be due to the diffusion of Gd from the GGG substrate into YIG observed by EDS [see Fig. 1(i)].

Further information on the magnetization of YIG(t_{YIG})/Pt(1.9) was obtained using x-ray absorption spectroscopy and x-ray magnetic circular dichroism (XMCD) at the L_3 and L_2 absorption edges of Fe. The x-ray absorption spectra of rep-
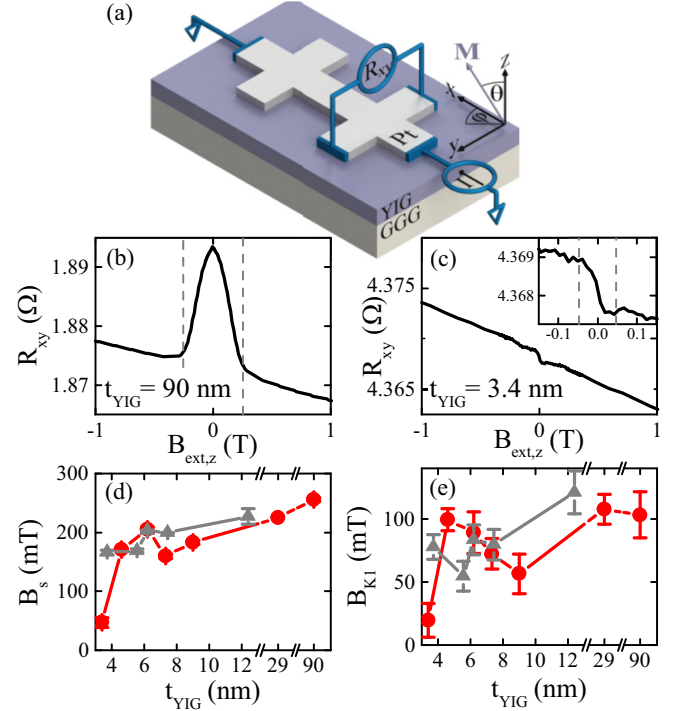

FIG. 5. (a) Schematic of the Hall bar and coordinate system. OOP field scans for the (b) thickest (90 nm) and (c) thinnest (3.4 nm) YIG thickness from series SMR 1. From these scans, the out-of-plane saturation field B_s was determined as indicated by the dashed line and summarized in (d) as a function of YIG thickness. (e) Easy-plane anisotropy field $B_{K_1} = B_s - \mu_0 M_s$. Data shown for sample series SMR 1 (red) and SMR 2 (grey).

resentative YIG(3.7,12.4,86.7)/Pt(1.9) samples present a very similar line shape [Fig. 4(c)], which implies that the chemical environment of the Fe atoms does not change substantially with thickness. The XMCD asymmetry, however, decreases in the thinner samples [Fig. 4(d)], consistent with the behavior of M_s discussed above. These data confirm that our samples are magnetic throughout the entire thickness range and suggest that the reduction of M_s is not due to defective Fe sites.

IV. MAGNETIC ANISOTROPY

To probe the magnetic anisotropy, we performed measurements of the transverse SMR [14,15] as a function of magnitude and orientation of the external magnetic field B_{ext}. Our data evidence the presence of an easy-plane anisotropy field, B_{K_1}, which adds to the demagnetization field to favor the in-plane magnetization, as well as of an easy-axis field B_{K_2}, which favors a particular in-plane direction that varies from sample to sample.

A. Transverse SMR measurements

A sketch of the Hall bar structure employed for the SMR measurements is presented in Fig. 5(a). We used an ac current $I = I_0 \sin(\omega t)$, modulated at a frequency $\omega/2\pi = 10$ Hz, and acquired the longitudinal and transverse (Hall) resistances [52,53]. To extract the magnetization orientation, we consider

here only the transverse resistance, R_{xy}, which is sensitive to all three Cartesian components of the magnetization due to the SMR effect [15]. We performed two types of measurements. In the first type, which we call an IP angle scan, we vary the in-plane angle of the applied magnetic field B_{ext}; in the second type, which we call an OOP field scan, we ramp B_{ext} applied out of plane. For both cases, it is convenient to use spherical coordinates: we define φ_B as the azimuthal angle between B_{ext} and I and φ as the azimuthal angle between the magnetization and I, whereas the polar angles of B_{ext} and the magnetization with respect to the surface normal are θ_B and θ, respectively [Fig. 5(a)].

In the IP angle scan ($\theta = \pi/2$), R_{xy} is determined solely by the planar Hall-like (PHE) contribution from the SMR, leading to

$$R_{xy} = R_{PHE} \sin(2\varphi), \tag{1}$$

where R_{PHE} is the planar Hall-like coefficient. In this type of experiment, we record R_{xy} as a function of φ_B for different B_{ext}. For fields large enough to saturate the magnetization along the field direction, we can assume $\varphi = \varphi_B$ and hence $R_{xy} = R_{PHE} \sin(2\varphi_B)$. Conversely, for external fields small enough such that $\varphi \neq \varphi_B$, R_{xy} will deviate from the $\sin(2\varphi_B)$ curve. By adopting a macrospin model assuming in-plane uniaxial magnetic anisotropy and comparing the resulting PHE from Eq. (1) with our data, we can determine quite accurately the easy-axis direction as well as the magnitude of the in-plane magnetic anisotropy energy.

In the OOP field scans, R_{xy} depends on the ordinary Hall effect (OHE) and anomalous Hall-like (AHE) contribution from the SMR, which is proportional to the out-of-plane component of magnetization [15]. We thus have

$$R_{xy} = R_{OHE} B_{ext} \cos \theta_B + R_{AHE} \cos \theta, \tag{2}$$

where R_{OHE} and R_{AHE} are the OHE and AHE coefficients, respectively. When ramping the OOP field, the contribution due to R_{OHE} continuously increases, whereas the contribution due to R_{AHE} saturates as the magnetization is fully aligned out of plane. The corresponding saturation field B_s can be used to determine the out-of-plane magnetic anisotropy knowing the value of M_s. All measurements were performed at room temperature using a current density in the low 10^5 A/cm^2 range.

B. Easy-plane anisotropy

The easy-plane anisotropy field was determined by comparing the hard-axis (out-of-plane) saturation field B_s measured by the Hall resistance with the demagnetizing field $\mu_0 M_s$ estimated using SQUID. Figures 5(b) and 5(c) show the results of OOP field scans for the thickest (90 nm) and thinnest (3.4 nm) YIG/Pt(3) samples. In both cases, we identify B_s (dashed line) as the field above which only the ordinary Hall effect contributes to the (linear) increase of R_{xy} with increasing field. Note that, for YIG(90)/Pt(3), we observe a bell-shaped curve that is due to the PHE during the reorientation of magnetic domains from the initial in-plane to the final out-of-plane orientation at B_s. Figure 5(d) reports the estimated values of B_s for all thicknesses. In all cases, we find that B_s is significantly larger than $\mu_0 M_s$ reported in Fig. 4(a).

We attribute this difference to an easy-plane anisotropy field, $B_{K_1} = B_s - \mu_0 M_s$, which favors in-plane magnetization. The magnitude of B_{K_1} varies in the range 50–100 mT (except for the thinnest sample). This additional easy-plane anisotropy is of the same order of magnitude as in previous studies [27,36], where it was attributed to a rhombohedral unit cell distortion along the [111] direction by $\approx$1%. Interestingly, the thinnest sample shows a drastically reduced B_{K_1} compared to the thicker ones, suggesting that very thin YIG films with $t_{YIG} \leqslant$ 3.4 nm tend to develop out-of-plane magnetic anisotropy [38]. This tendency, however, is not sufficient to induce an out-of-plane easy axis, as verified by SQUID measurements as a function of out-of-plane field. The reduction of B_{K_1} may also explain the absence of the bell-shaped PHE contribution to R_{xy} observed in Fig. 5(c).

C. In-plane uniaxial anisotropy

The in-plane uniaxial anisotropy field B_{K_2} is determined by measuring IP angle scans of R_{xy} for different constant values of B_{ext}. By choosing B_{ext} below the in-plane saturation field and fitting R_{xy} as a function of φ_B using a macrospin model, we determine the orientation of the in-plane easy axis as well as the magnitude of B_{K_2}. The black circles in Figs. 6(a)–6(c) show R_{xy} as a function of φ_B for three representative YIG thicknesses (90, 9, and 3.4 nm). For all three samples, we identify the $\sin(2\varphi)$ behavior expected from Eq. (1) for $B_{ext} >$ 7.2 mT [upper panels in Figs. 6(a)–6(c)]. When reducing B_{ext}, deviations from this line shape occur, indicating that the magnetization no longer follows the external magnetic field. This behavior is most pronounced for fields of only tens of microteslas [lower panels in Figs. 6(a)–6(c)]. For such low fields, we observe two prominent jumps of R_{xy} separated by 180°, which we attribute to the magnetization switching abruptly from one quadrant to the opposite one during an IP angle scan in proximity to the hard axis. These jumps, which occur at different φ_B for the three samples, indicate the presence of in-plane uniaxial anisotropy.

In order to quantify the in-plane uniaxial anisotropy, we perform macrospin simulations of R_{xy} assuming the following energy functional:

$$E = -M_s \vec{m} \cdot \vec{B}_{ext} + M_s B_{K_2} \sin^2(\varphi - \varphi_{EA}), \tag{3}$$

where $\vec{m}$ is the magnetization unit vector and φ_{EA} defines the angle of the easy axis with respect to the [1$\bar{1}$0] crystal axis. Expressing $\vec{m}$ and $\vec{B}_{ext}$ in spherical coordinates, i.e., $\vec{m} = (\sin \theta \cos \varphi, \sin \theta \sin \varphi, \cos \theta)$ and $\vec{B}_{ext} = B_{ext}(\sin \theta_B \cos \varphi_B, \sin \theta_B \sin \varphi_B, \cos \theta_B)$, and taking $\theta = \theta_B = \pi/2$, we can calculate the equilibrium position of the magnetization as a function of $B_{ext}, \varphi_B, B_{K_2}$, and φ_{EA}. This calculation results in a set of values $\varphi(\varphi_B)$ that can be used to simulate R_{xy} using Eq. (1). The planar Hall constants R_{PHE} required for the simulations are obtained by fitting Eq. (1) to the saturated data sets. Finally, we fit $R_{xy}(\varphi_B)$ keeping B_{K_2} and φ_{EA} as free parameters. The fits, shown as red lines in Figs. 6(a)–6(c), reproduce the main features (line shape and jumps) of R_{xy} quite accurately, indicating that our method is appropriate to measure weak anisotropy fields in YIG. The resulting values of φ_{EA} and B_{K_2} are shown by the symbols in Figs. 6(d) and 6(e), respectively.
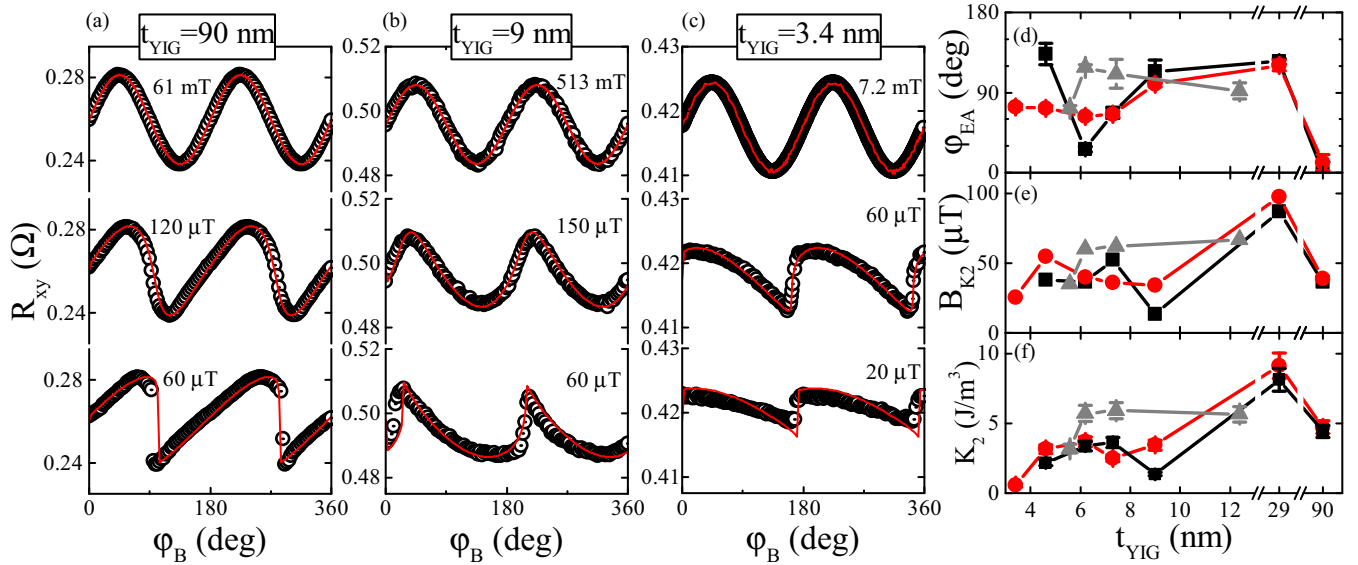
FIG. 6. Transverse resistance R_{xy} as a function of azimuthal orientation of the external magnetic field, φ_B, for different thicknesses in (a–c). The data are shown by black symbols, the macrospin simulations by red solid lines. (d) Easy-axis orientation, φ_{EA}, relative to the $[1\bar{1}0]$ crystal axis. (e) Effective uniaxial anisotropy field B_{K_2} and (f) in-plane uniaxial energy $M_s B_{K_2}$ as a function of YIG thickness. Black and red points show the results for two different Hall bars patterned on the same chips of series SMR 1; grey triangles are results obtained on Hall bars of series SMR 2.

The data for the series SMR 1 (red) in Fig. 6(d) appear to follow a pattern in the orientation of the easy axis as a function of thickness. Very thin samples with $t_{YIG} \leqslant 7.2$ nm have $\varphi_{EA} \approx 60°$, whereas intermediate thicknesses in the range $9 \leqslant t_{YIG} \leqslant 29$ nm have $\varphi_{EA} \approx 120°$ and the thickest sample, $t_{YIG} = 90$ nm, has $\varphi_{EA} \approx 0°$. While these orientations correspond to the threefold symmetry of the (111) plane, measurements on different sets of samples show that this correspondence is likely coincidental. Measurements performed on devices patterned on the same chip (black squares) of series SMR 1 as well as on one device of the series SMR 2 (grey triangles) reveal uncorrelated variations of φ_{EA} relative to the SMR 1 series, particularly for $t_{YIG} < 10$ nm. A variation of φ_{EA} for samples grown on the same chip has also been observed in thicker YIG films [27] and is most likely due to inhomogeneities of process parameters such as, e.g., the temperature of the sample surface during deposition, which could lead to local strain differences.

Figure 6(e) shows B_{K_2} as a function of t_{YIG}. Most values are close to 50 μT, with minima and maxima of about 20 and 100 μT, respectively. Combined with the thickness-dependent saturation magnetization from Fig. 4(a), we obtain a magnetic anisotropy energy $K_2 = M_s B_{K_2}$ in the range of 0.1 to 10 J/m^3 [Fig. 6(f)]. K_2 is more than two orders of magnitude smaller than the first-order cubic anisotropy constant of bulk YIG (-610 J/m^3) [22], which reinforces the hypothesis of an extrinsic origin of the uniaxial anisotropy reported here.

Our observation of uniaxial anisotropy agrees with previous studies of YIG films grown by PLD on GGG [27,31,36,54]. From a crystallographic point of view, however, uniaxial anisotropy is not expected for the YIG(111) plane. Rather, for an ideal (111) crystal plane, one would expect a threefold anisotropy due to the cubic magnetocrystalline anisotropy of bulk YIG [55]. This becomes obvi-

ous when translating the first-order magnetocrystalline energy term of cubic crystals ($E_{cubic} \propto \alpha_1^2 \alpha_2^2 + \alpha_2^2 \alpha_3^2 + \alpha_3^2 \alpha_1^2$, where $\alpha_{1,2,3}$ are the directional cosines with respect to the main crystallographic axes) into the coordinate system of the (111) plane (θ with respect to the [111] direction and, for simplicity, φ with respect to the $[11\bar{2}]$ direction), giving

$$E_{cubic} \propto \frac{1}{4} \sin^4 \theta + \frac{1}{3} \cos^4 \theta + \frac{\sqrt{2}}{3} \sin^3 \theta \cos \theta \cos 3\varphi. \quad (4)$$

In order for the threefold anisotropy to appear [last term in Eq. (4)], the magnetization has to have a small out-of-plane component ($\theta \neq \pi/2$). Whereas this can be generally guaranteed in bulk crystals, in thin films the demagnetizing field and B_{K_1} force $\theta = \pi/2$, resulting in the absence of threefold cubic anisotropy. The origin of the in-plane uniaxial anisotropy thus remains to be explained. Our XRD measurements reveal no significant in-plane strain anisotropy within the accuracy of the reciprocal space maps in Figs. 1(d) and 1(e). The small amplitude of B_{K_2} and the intra- and interseries variations of φ_{EA} suggest that this anisotropy may originate from local inhomogeneities of the growth or patterning parameters, which should therefore be taken into account for the fabrication of YIG-based devices.

V. MAGNETIC DOMAINS

The domain structure in bulk YIG is of flux-closure type with magnetic orientation dictated by the easy axes along the [111]-equivalent directions [56,57]. In the case of a defect-free YIG crystal, the domains can be as large as the sample
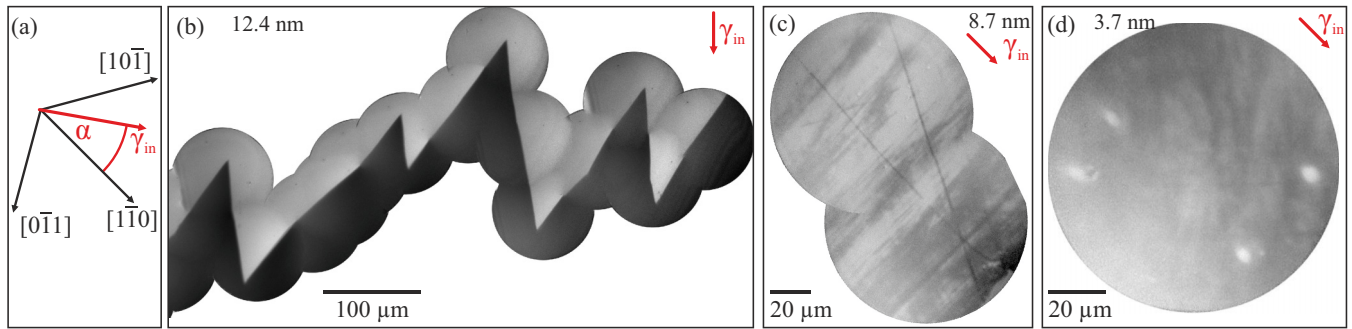
FIG. 7. (a) Schematics of the direction of the incoming x-ray beam (red arrow) relative to the crystal axes in the XPEEM setup. (b–d) Domain structure of YIG/Pt(1.9) bilayers with t_{YIG} = 12.4, 8.7, and 3.7 nm observed by XPEEM. The gray scale contrast corresponds to different in-plane orientations of the magnetization.

itself, apart from the flux closure domains at the edges. Dislocations and strain favor the formation of smaller domains [57]. External strain and local stress due to dislocations can result in a variety of magnetic configurations such as cylindrical domains [57] and complex local patterns [56,58]. Moreover, dislocations serve as pinning sites for domain walls [59]. The domain walls observed at the surface of YIG single crystals are usually of the Bloch type and several micrometers wide [56,60].

In the following, we characterize the domain structure of YIG thin films using XPEEM. The samples are YIG(t_{YIG})/Pt(1.9) bilayers with thickness down to t_{YIG} = 3.7 nm, as described for the XPEEM series in Table I. The measurements were performed at the SIM beamline of the Swiss Light Source [61] by tuning the x-ray energy to obtain the maximum XMCD contrast at the Fe L_3 edge (710 eV) and using a circular field of view with a diameter of 100 or 50 μm. Magnetic contrast images were obtained by dividing pixel-wise consecutive images recorded with circular left- and right-polarized x-rays. Prior to imaging, the samples were demagnetized in an ac magnetic field applied along the surface normal.

A. Domain structure

Figure 7 shows representative XPEEM images of the magnetic domains of 12.4-, 8.7-, and 3.7-nm-thick YIG. Thicker films (t_{YIG} = 86.7, 28.5, and 12.4 nm) present qualitatively similar domain structures such as those shown in Fig. 7(b) for the 12.4-nm-thick film. The domains in these thicker films extend over hundreds of micrometers and meet head-on, separated by domain walls with characteristic zigzag boundaries. Such walls are typical of thin films with in-plane uniaxial anisotropy, where the zigzag amplitude and period depends on the balance between magnetostatic charge density and domain wall energy, as well as on the process of domain formation [62–64]. Note that the two sides of each zigzag are asymmetric, as found in ion-implanted garnets with uniaxial and trigonal in-plane anisotropy [65]. The length and opening angle of the zigzags increase and decrease, respectively, with increasing film thickness, similar to the trend reported for amorphous Ga-doped Co films with weak uniaxial anisotropy [65]. In a quantitative model based on the mentioned energy

balance [66], both quantities correlate with M_s in a positive and negative manner, respectively. This trend is in agreement with the increase of M_s reported in Fig. 4(a).

The domain morphology changes abruptly in films thinner than 12.4 nm. YIG films with t_{YIG} = 8.7 and 3.7 nm present much smaller domains, which extend only for tens of micrometers and have a weaving pattern, as shown in Figs. 7(c) and 7(d), respectively. In the 8.7-nm-thick film, the domains elongate along the [11$\bar{2}$] direction, likely due to the presence of in-plane uniaxial anisotropy. In the 3.7-nm-thick film, the domains are more irregular and do not present such a strong preferred orientation, consistent with the reduced demagnetizing field and smaller in-plane anisotropy reported for this thickness [see Figs. 5(e) and 6(f), respectively].

B. Domain walls

XPEEM images provide sufficient contrast to analyze the domain walls of films with $t_{YIG} \geqslant$ 12.4 nm, which consist of straight segments along the zigzag boundary shown in Fig. 7(b). Figures 8(a)–8(c) show details of the 180° domain walls that delimit the edges of the zigzag domains in 86.7-, 28.5-, and 12.4-nm-thick YIG. Line cuts of the XMCD intensity across the walls are shown in Figs. 8(d)–8(f). As the XMCD intensity scales with the projection of the magnetization onto the x-ray incidence direction (red arrows), the "overshoot" of the XMCD intensity in the central wall region compared to the side regions in Figs. 8(d) and 8(e) indicates that the magnetization rotates in the plane of the films. This observation is consistent with the Néel wall configuration expected for thin films with in-plane magnetic anisotropy [64], and contrasts with the Bloch walls reported at the surface of bulk YIG crystals [56,60]. The walls appear to have a core region, corresponding to the length over which the magnetic contrast changes most abruptly, which is about 1–2 μm wide, and a tail that extends over several micrometers, which is a typical feature of Néel walls in soft films with in-plane magnetization [64].

The domain wall in Fig. 8(b) shows an inversion of the magnetic contrast at a vortexlike singular point in the middle of the image. Such a contrast inversion reveals that the wall is composed of different segments with opposite rotation mode of the magnetization, i.e., opposite chirality.
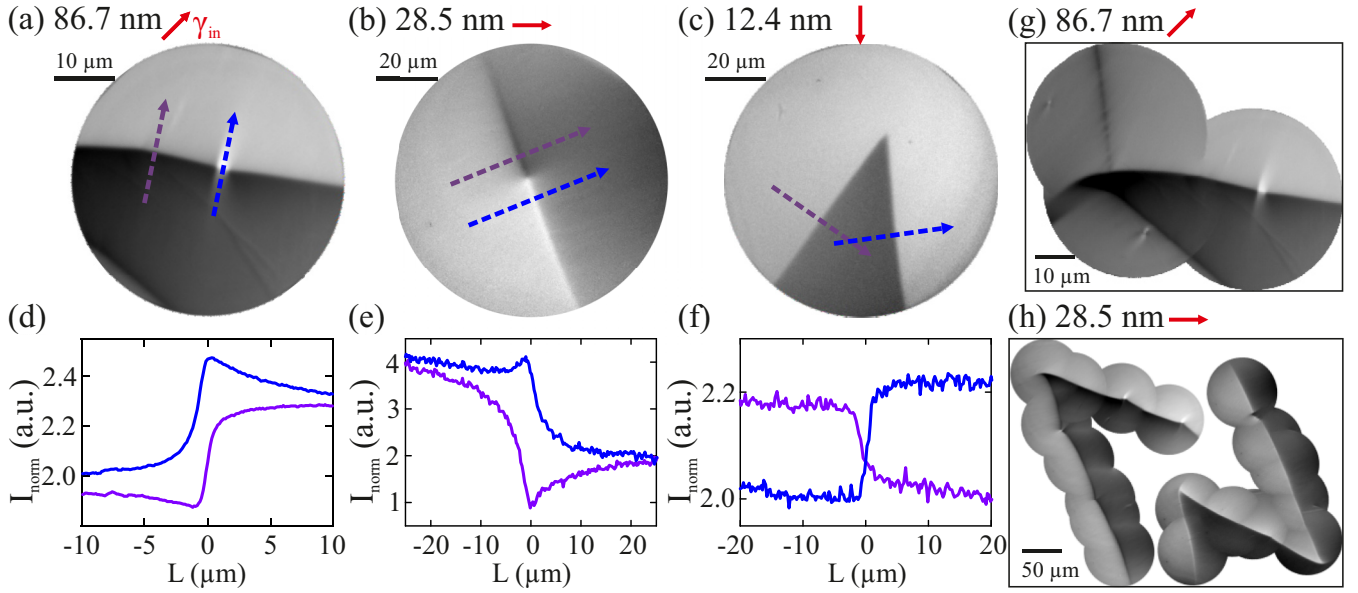
FIG. 8. XPEEM images of domain walls in (a) 86.7-, (b) 28.5-, and (c) 12.4-nm-thick YIG. The arrows indicate the x-ray incidence direction. (d–f) Line profiles of the walls corresponding to the dashed lines in (a–c). (g, h) Details of the apices of the zigzag domains in 86.7- and 28.5-nm-thick YIG. The samples are oriented with the crystal axes defined in Fig. 7(a).

The singular point that separates two consecutive segments is a so-called Bloch point, which can extend from the top to the bottom of the film, forming a Bloch line. Such features have smaller dimensions compared to the wall width and are therefore considered to favor the pinning of domain walls at defects, thus acting as a source of coercivity in soft magnetic materials [64].

Figures 8(g) and 8(h) further show that the domain walls at the apices of the zigzag domains in the 86.7- and 28.5-nm-thick films have a curved shape. This feature suggests that the domains are indeed pinned at defect sites, likely of structural origin [57,59]. Finally, we note that the domain features reported here move under the influence of an external in-plane magnetic field of the order of few milliteslas, as well as by ramping the out-of-plane field that compensates the magnetic field of the XPEEM lenses at the sample spot.

VI. CONCLUSIONS

Our study shows that the magnetic properties and domain configuration of epitaxial YIG(111) films grown by PLD on GGG and capped by Pt depend strongly on the thickness of the YIG layer. Despite the high structural and interface quality indicated by XRD and TEM, the saturation magnetization decreases from $M_s = 122$ kA/m (15% below bulk value) in 90-nm-thick YIG to 22 kA/m in 3.4-nm-thick YIG. The gradual decrease of M_s suggests a continuous degradation of M_s rather than the formation of a dead layer. All films except the thinner one ($t_{YIG} = 3.4$ nm) present a rather strong easy-plane anisotropy in addition to the shape anisotropy, of the order of 10^3–10^4 J/m^3. Additionally, all films except the thinner one present weak in-plane uniaxial anisotropy, of the order of 3–10 J/m^3. This anisotropy defines a preferential orientation of the magnetization in each sample, which, however, is found

to vary not only as a function of thickness but also between samples with the same nominal thickness and even for samples patterned on the same substrate. The origin of this variation is tentatively attributed to local inhomogeneities of the growth or patterning process, which could lead to small strain differences not detectable by XRD. Besides these findings, we underline the fact that SMR measurements performed for external magnetic fields smaller or comparable to the effective anisotropy fields allow for the accurate characterization of both the magnitude and direction of the magnetic anisotropy of YIG/Pt bilayers, with an accuracy better than 10 μT.

YIG films with $t_{YIG} = 10$–90 nm present large, millimeter-size, in-plane domains delimited by zigzag boundaries and Néel domain walls. The apices of the zigzags are pinned by defects, whereas the straight sections of the walls incorporate Bloch-like singularities, which separate regions of the walls with opposite magnetization chirality. The domain morphology changes abruptly in the thinner films. Whereas the 8.7-nm-thick YIG presents elongated domains that are tens of micrometers long, the domains in the 3.7-nm-thick YIG are smaller and more irregular, consistent with the reduction of the easy-plane and uniaxial anisotropy reported for this sample. Our measurements indicate that the performance of YIG-based spintronic devices may be strongly influenced by the thickness as well as by local variations of the YIG magnetic properties.

[1] K.-i. Uchida, H. Adachi, T. Ota, H. Nakayama, S. Maekawa, and E. Saitoh, Appl. Phys. Lett. **97**, 172505 (2010).

[2] M. Schreier, N. Roschewsky, E. Dobler, S. Meyer, H. Huebl, R. Gross, and S. T. Goennenwein, Appl. Phys. Lett. **103**, 242404 (2013).

[3] W. Wang, S. Wang, L. Zou, J. Cai, Z. Sun, and J. Sun, Appl. Phys. Lett. **105**, 182403 (2014).

[4] N. Vlietstra, J. Shan, B. J. van Wees, M. Isasa, F. Casanova, and J. Ben Youssef, Phys. Rev. B **90**, 174436 (2014).

[5] B. Heinrich, C. Burrowes, E. Montoya, B. Kardasz, E. Girt, Y.-Y. Song, Y. Sun, and M. Wu, Phys. Rev. Lett. **107**, 066604 (2011).

[6] V. Castel, N. Vlietstra, B. J. van Wees, and J. B. Youssef, Phys. Rev. B **86**, 134419 (2012).

[7] H. L. Wang, C. H. Du, Y. Pu, R. Adur, P. C. Hammel, and F. Y. Yang, Phys. Rev. B **88**, 100406(R) (2013).

[8] V. Castel, N. Vlietstra, B. J. van Wees, and J. Ben Youssef, Phys. Rev. B **90**, 214434 (2014).

[9] L. Cornelissen, J. Liu, R. Duine, J. B. Youssef, and B. Van Wees, Nat. Phys. **11**, 1022 (2015).

[10] L. J. Cornelissen and B. J. van Wees, Phys. Rev. B **93**, 020403(R) (2016).

[11] L. J. Cornelissen, K. J. H. Peters, G. E. W. Bauer, R. A. Duine, and B. J. van Wees, Phys. Rev. B **94**, 014412 (2016).

[12] S. Emori, A. Matyushov, H.-M. Jeon, C. J. Babroski, T. Nan, A. M. Belkessam, J. G. Jones, M. E. McConney, G. J. Brown, B. M. Howe *et al.*, Appl. Phys. Lett. **112**, 182406 (2018).

[13] J. Sklenar, W. Zhang, M. B. Jungfleisch, W. Jiang, H. Chang, J. E. Pearson, M. Wu, J. B. Ketterson, and A. Hoffmann, Phys. Rev. B **92**, 174406 (2015).

[14] H. Nakayama, M. Althammer, Y.-T. Chen, K. Uchida, Y. Kajiwara, D. Kikuchi, T. Ohtani, S. Geprägs, M. Opel, S. Takahashi *et al.*, Phys. Rev. Lett. **110**, 206601 (2013).

[15] Y.-T. Chen, S. Takahashi, H. Nakayama, M. Althammer, S. T. B. Goennenwein, E. Saitoh, and G. E. W. Bauer, Phys. Rev. B **87**, 144411 (2013).

[16] C. Hahn, G. de Loubens, O. Klein, M. Viret, V. V. Naletov, and J. Ben Youssef, Phys. Rev. B **87**, 174417 (2013).

[17] M. Althammer, S. Meyer, H. Nakayama, M. Schreier, S. Altmannshofer, M. Weiler, H. Huebl, S. Geprägs, M. Opel, R. Gross *et al.*, Phys. Rev. B **87**, 224401 (2013).

[18] N. Vlietstra, J. Shan, V. Castel, J. Ben Youssef, G. Bauer, and B. Van Wees, Appl. Phys. Lett. **103**, 032401 (2013).

[19] M. Schreier, T. Chiba, A. Niedermayr, J. Lotze, H. Huebl, S. Geprägs, S. Takahashi, G. E. W. Bauer, R. Gross, and S. T. B. Goennenwein, Phys. Rev. B **92**, 144411 (2015).

[20] Z. Fang, A. Mitra, A. Westerman, M. Ali, C. Ciccarelli, O. Cespedes, B. Hickey, and A. Ferguson, Appl. Phys. Lett. **110**, 092403 (2017).

[21] R. Pearson, in *Proceedings of the Seventh Conference on Magnetism and Magnetic Materials* (Springer, Berlin, 1962), pp. 1236–1242.

[22] P. Hansen, K. Enke, and G. Winkler, in *Part A: Garnets and Perovskites* (Springer, Berlin, 1978), pp. 82–86.

[23] D. Heinz, P. Besser, J. Owens, J. Mee, and G. Pulliam, J. Appl. Phys. **42**, 1243 (1971).

[24] A. Thiaville, F. Boileau, J. Miltat, and L. Arnaud, J. Appl. Phys. **63**, 3153 (1988).

[25] F. V. Lisovskii, E. G. Mansvetova, M. P. Temiryazeva, and A. G. Temiryazev, JETP Lett. **96**, 596 (2013).

[26] P. Pirro, T. Brächer, A. Chumak, B. Lägel, C. Dubs, O. Surzhenko, P. Görnert, B. Leven, and B. Hillebrands, Appl. Phys. Lett. **104**, 012402 (2014).

[27] B. B. Krichevtsov, S. V. Gastev, S. M. Suturin, V. V. Fedorov, A. M. Korovin, V. E. Bursian, A. G. Banshchikov, M. P. Volkov, M. Tabuchi, and N. S. Sokolov, Sci. Technol. Adv. Mater. **18**, 351 (2017).

[28] H. Wang, C. Du, P. C. Hammel, and F. Yang, Phys. Rev. B **89**, 134404 (2014).

[29] J. F. K. Cooper, C. J. Kinane, S. Langridge, M. Ali, B. J. Hickey, T. Niizeki, K. Uchida, E. Saitoh, H. Ambaye, and A. Glavic, Phys. Rev. B **96**, 104404 (2017).

[30] P. Dorsey, S. Bushnell, R. Seed, and C. Vittoria, J. Appl. Phys. **74**, 1242 (1993).

[31] S. A. Manuilov, S. Khartsev, and A. M. Grishin, J. Appl. Phys. **106**, 123917 (2009).

[32] S. A. Manuilov and A. M. Grishin, J. Appl. Phys. **108**, 013902 (2010).

[33] Y. Sun, Y.-Y. Song, H. Chang, M. Kabatek, M. Jantz, W. Schneider, M. Wu, H. Schultheiss, and A. Hoffmann, Appl. Phys. Lett. **101**, 152405 (2012).

[34] O. d'Allivy Kelly, A. Anane, R. Bernard, J. Ben Youssef, C. Hahn, A. H. Molpeceres, C. Carrétéro, E. Jacquet, C. Deranlot, P. Bortolotti *et al.*, Appl. Phys. Lett. **103**, 082408 (2013).

[35] M. Onbasli, A. Kehlberger, D. Kim, G. Jakob, M. Kläui, A. Chumak, B. Hillebrands, and C. Ross, APL Mater. **2**, 106102 (2014).

[36] N. Sokolov, V. Fedorov, A. Korovin, S. Suturin, D. Baranov, S. Gastev, B. Krichevtsov, K. Y. Maksimova, A. Grunin, V. Bursian *et al.*, J. Appl. Phys. **119**, 023903 (2016).

[37] C. Hauser, T. Richter, N. Homonnay, C. Eisenschmidt, M. Qaid, H. Deniz, D. Hesse, M. Sawicki, S. G. Ebbinghaus, and G. Schmidt, Sci. Rep. **6**, 20827 (2016).

[38] E. Popova, N. Keller, F. Gendron, L. Thomas, M.-C. Brianso, M. Guyot, M. Tessier, and S. Parkin, J. Vac. Sci. Technol. A **19**, 2567 (2001).

[39] A. Mitra, O. Cespedes, Q. Ramasse, M. Ali, S. Marmion, M. Ward, R. Brydson, C. Kinane, J. Cooper, S. Langridge *et al.*, Sci. Rep. **7**, 11774 (2017).

[40] J. M. Gomez-Perez, S. Vélez, L. McKenzie-Sell, M. Amado, J. Herrero-Martín, J. López-López, S. Blanco-Canosa, L. E. Hueso, A. Chuvilin, J. W. A. Robinson *et al.*, Phys. Rev. Appl. **10**, 044046 (2018).

[41] M. B. Jungfleisch, A. V. Chumak, A. Kehlberger, V. Lauer, D. H. Kim, M. C. Onbasli, C. A. Ross, M. Kläui, and B. Hillebrands, Phys. Rev. B **91**, 134407 (2015).

[42] M. Haertinger, C. H. Back, J. Lotze, M. Weiler, S. Geprägs, H. Huebl, S. T. B. Goennenwein, and G. Woltersdorf, Phys. Rev. B **92**, 054437 (2015).

[43] A. Kehlberger, U. Ritzmann, D. Hinzke, E.-J. Guo, J. Cramer, G. Jakob, M. C. Onbasli, D. H. Kim, C. A. Ross, M. B. Jungfleisch, B. Hillebrands, U. Nowak, and M. Kläui, Phys. Rev. Lett. **115**, 096602 (2015).

[44] A. Temiryazev, M. Tikhomirova, and I. Fedorov, J. Magn. Magn. Mater. **258**, 580 (2003).

[45] W. Xia, Y. Chun, S. Aizawa, K. Yanagisawa, K. M. Krishnan, D. Shindo, and A. Tonomura, J. Appl. Phys. **108**, 123919 (2010).

[46] S. Geller and M. Gilleo, J. Phys. Chem. Solids **3**, 30 (1957).

[47] H. Chang, T. Liu, D. Reifsnyder Hickey, P. A. P. Janantha, K. A. Mkhoyan, and M. Wu, APL Mater. **5**, 126104 (2017).

[48] C. Colliex, T. Manoubi, and C. Ortiz, Phys. Rev. B **44**, 11402 (1991).

[49] P. Hansen, P. Röschmann, and W. Tolksdorf, J. Appl. Phys. **45**, 2728 (1974).

[50] E. Popova, N. Keller, F. Gendron, M. Guyot, M.-C. Brianso, Y. Dumond, and M. Tessier, J. Appl. Phys. **90**, 1422 (2001).

[51] Y. Dumont, N. Keller, E. Popova, D. Schmool, S. Bhattacharya, B. Stahl, M. Tessier, and M. Guyot, J. Appl. Phys. **97**, 10G108 (2005).

[52] K. Garello, I. M. Miron, C. O. Avci, F. Freimuth, Y. Mokrousov, S. Blügel, S. Auffret, O. Boulle, G. Gaudin, and P. Gambardella, Nat. Nanotechnol. **8**, 587 (2013).

[53] C. O. Avci, K. Garello, A. Ghosh, M. Gabureac, S. F. Alvarado, and P. Gambardella, Nat. Phys. **11**, 570 (2015).

[54] C. T. Wang, X. F. Liang, Y. Zhang, X. Liang, Y. P. Zhu, J. Qin, Y. Gao, B. Peng, N. X. Sun, and L. Bi, Phys. Rev. B **96**, 224403 (2017).

[55] S.-K. Chung and M. W. Muller, J. Magn. Magn. Mater. **1**, 114 (1975).

[56] J. Basterfield, J. Appl. Phys. **39**, 5521 (1968).

[57] V. Vlasko-Vlasov, L. Dedukh, and V. Nikitenko, Zh. Eksp. Teor. Fiz. **71**, 2291 (1976).

[58] V. Vlasko-Vlasov, L. Dedukh, and V. Nikitenko, JETP **38**, 184 (1974).

[59] V. Vlasko-Vlasov, L. Dedukh, and V. Nikitenko, Phys. Status Solidi A **29**, 367 (1975).

[60] M. Labrune, J. Miltat, and M. Kléman, J. Appl. Phys. **49**, 2013 (1978).

[61] L. Le Guyader, A. Kleibert, A. F. Rodríguez, S. El Moussaoui, A. Balan, M. Buzzi, J. Raabe, and F. Nolting, J. Electron Spectrosc. Relat. Phenom. **185**, 371 (2012).

[62] C. Favieres, J. Vergara, and V. Madurga, J. Phys.: Condens. Matter **25**, 066002 (2013).

[63] S. Hamzaoui, M. Labrune, and I. Puchalska, Appl. Phys. Lett. **45**, 1246 (1984).

[64] A. Hubert and R. Schäfer, *Magnetic Domains: The Analysis of Magnetic Microstructures* (Springer, Berlin, 2008).

[65] M. Freiser, IBM J. Res. Dev. **23**, 330 (1979).

[66] M. Labrune, S. Hamzaoui, and I. Puchalska, J. Magn. Magn. Mater. **27**, 323 (1982).